CERN-ACC-2019-0041

Galina.Skripka@cern.ch
Giovanni.Iadarola@cern.ch

Beam-induced heat loads on the beam screens of the HL-LHC arcs

G. Skripka and G. Iadarola
CERN, Geneva, Switzerland

Keywords: LHC, HL-LHC, heat loads, arc, beam screen, impedance, electron cloud

Abstract

The heat load on the beam screens of cold magnets and drift sections in the HL-LHC arcs is estimated considering power deposition from impedance, synchrotron radiation and electron cloud. Estimates are given both for the standard 25 ns scheme and for the 8b+4e backup scheme.
These two beam structures can optionally be combined within the same filling scheme to find the best compromise between performance and heat load. For this purpose, a simple analytic model is derived, which allows determining the optimal share for a given target heat load.

Geneva, Switzerland
September, 2019

1 Introduction

Large beam-induced heat loads have been measured on the beam screens of the Large Hadron Collider (LHC), during operation with the nominal bunch spacing of 25 ns in Run 2. These heat loads are much larger than expected from impedance and synchrotron radiation. Several observations, in particular the fact that the load is reduced by a large factor when using the 50 ns bunch spacing, indicate that the source of the additional load is the electron cloud effect [1–3].
Large differences in the measured heat loads are observed among the eight LHC arcs. This feature is not expected, as the arcs are by design identical, and is so far unexplained. A dedicated inter-departmental task force has been formed to investigate this issue.
In view of the High-Luminosity LHC upgrade project (HL-LHC) it is important to accurately predict how the arc heat loads will behave when increasing the bunch population up to 2.3×10^{11} p/bunch [4,5] .
This note presents simulation studies performed with the PyECLOUD macro-particle code [6] in order to investigate the e-cloud formation in the different components of the LHC arcs for different beam configurations and surface properties and assess its impact on the heat loads.
The two following scenarios are considered:

- The **nominal HL-LHC filling scheme** illustrated in Fig. 1, which is composed of trains of 72 bunches with 25 ns spacing and allows storing 2760 bunches per ring;
- The **8b+4e filling scheme** illustrated in Fig. 2, which is a backup scheme conceived in order to mitigate electron cloud effects [7]. It is composed of short trains of eight bunches interleaved with gaps of four empty slots and allows storing 1972 bunches per ring.

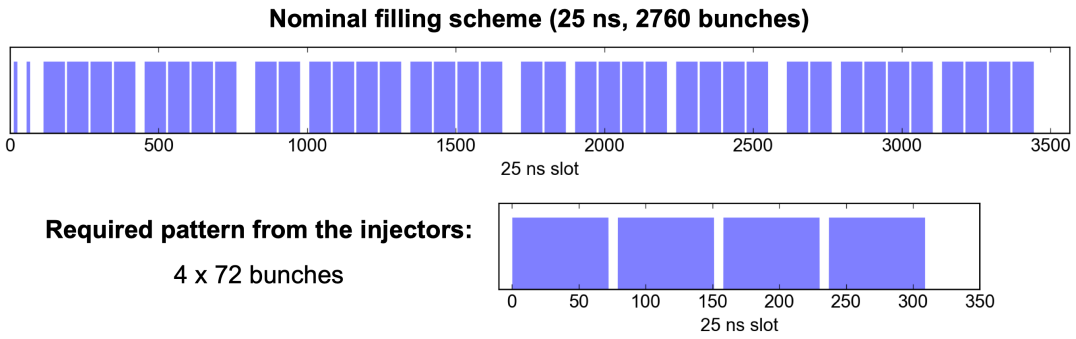

Figure 1: Standard 25 ns filling scheme using trains 72 bunches. The blue background marks the filled bunch slots.

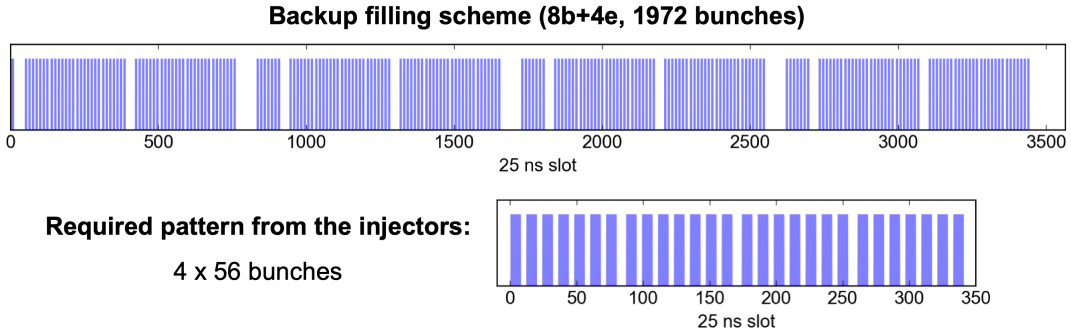

Figure 2: 8b+4e filling scheme made of trains of eight bunches. The blue background marks the filled bunch slots.

Table 1: Simulation parameters

Energy, GeV	450 and 7000
Beam type	standard 25 ns and 8b+4e
Bunch population, p	$0.1 - 2.5 \times 10^{11}$ (scanned)
RMS bunch length (Gaussian), m	0.09
Normalized transverse emittance, μm	2.5
Optics	HL-LHC v1.4
Bunch spacing, ns	25
Total number of bunches	2760 (std 25 ns) and 1972 (8b+4e)

2 E-cloud build-up simulations

PyECLOUD simulations have been performed for dipoles, quadrupoles and drift sections of the LHC arcs. The impact of shorter magnetic elements (e.g. corrector magnets) was shown to be negligible in previous studies [8]. A detailed description of the employed simulation model can be found in [8]. The modelling of the secondary electron emission process is based on [9].
The main beam parameters used in the simulations are summarized in Tab. 1 and are based on the operational scenarios described in [5]. For the injection energy cases the simulations were initialized with a small number of electrons compared to the expected saturation level. Primary electron generation via photoemission is instead used for the high energy cases [8].
A sufficiently long portion of the beam was simulated to ensure that the e-cloud reaches the saturation regime [10] within the simulation time span. As illustrated in Fig. 3, this required simulating a different number of trains depending on the Secondary Electron Yield (SEY). The total heat load and the total electron current on the chamber's wall are estimated by rescaling those produced from the last simulated train to the full number of bunches.
Simulations were performed for different values of the SEY parameter (called $\delta_{\max}$ in [9]) uniformly spaced in the range $1.0 - 1.6$ and for beam intensities in the range $(0.1 - 2.5) \times 10^{11}$ p/bunch, fully covering the operational range for the HL-LHC.

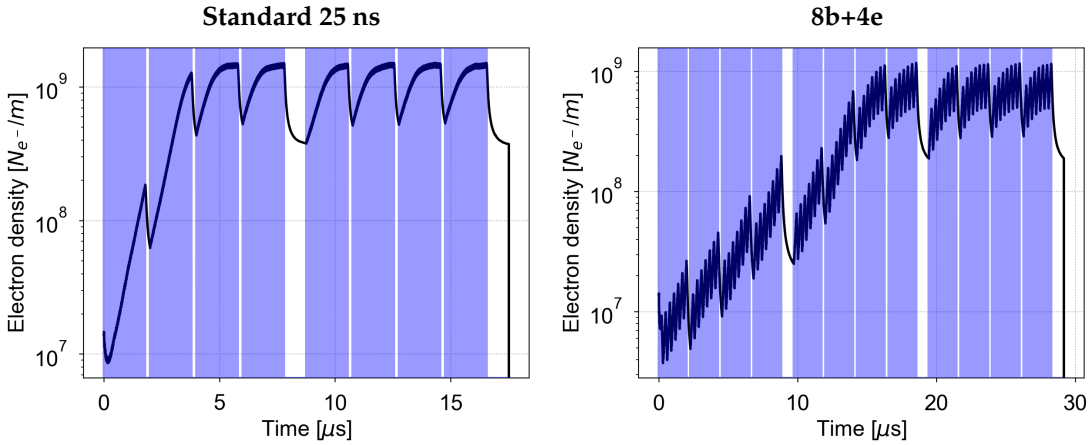

Figure 3: Accumulation of electrons in the chamber of a quadrupole, assuming SEY=1.25 for the standard 25 ns beam (left) and for the 8b+4e beam (right). The blue background marks the passing bunches.

The results of the PyECLOUD simulations are illustrated in Figs 4 - 11, which show the heat load and of the electron current on the chamber surface as a function of the bunch population and of the SEY, for all considered cases.
As expected, a significant reduction both in heat load and in electron current is observed for the 8b+4e case compared to the 25 ns case.
A significant increase from the 450 GeV to the 7 TeV beam energy is observed for the drift sections, more than for the dipole and the quadrupole magnets. This was already observed and explained in previous studies, showing that in the drifts the photoelectrons generated by the direct impact of the synchrotron radiation are not confined by the magnetic field in the region close to the sawtooth profile, but are free to move across the chamber and to contribute to the multipacting [11].
The quadrupole magnets tend to show significantly larger heat loads and electron currents compared to the dipole and drift cases, both at 450 GeV and 7 TeV and for the standard 25 ns and 8b+4e beam configurations. This is caused by "electron trapping" effects which occur due to the presence of a non-homogeneous magnetic fields. This increases the probability of electrons surviving between consecutive bunch passages and therefore enhances the multipacting [12].

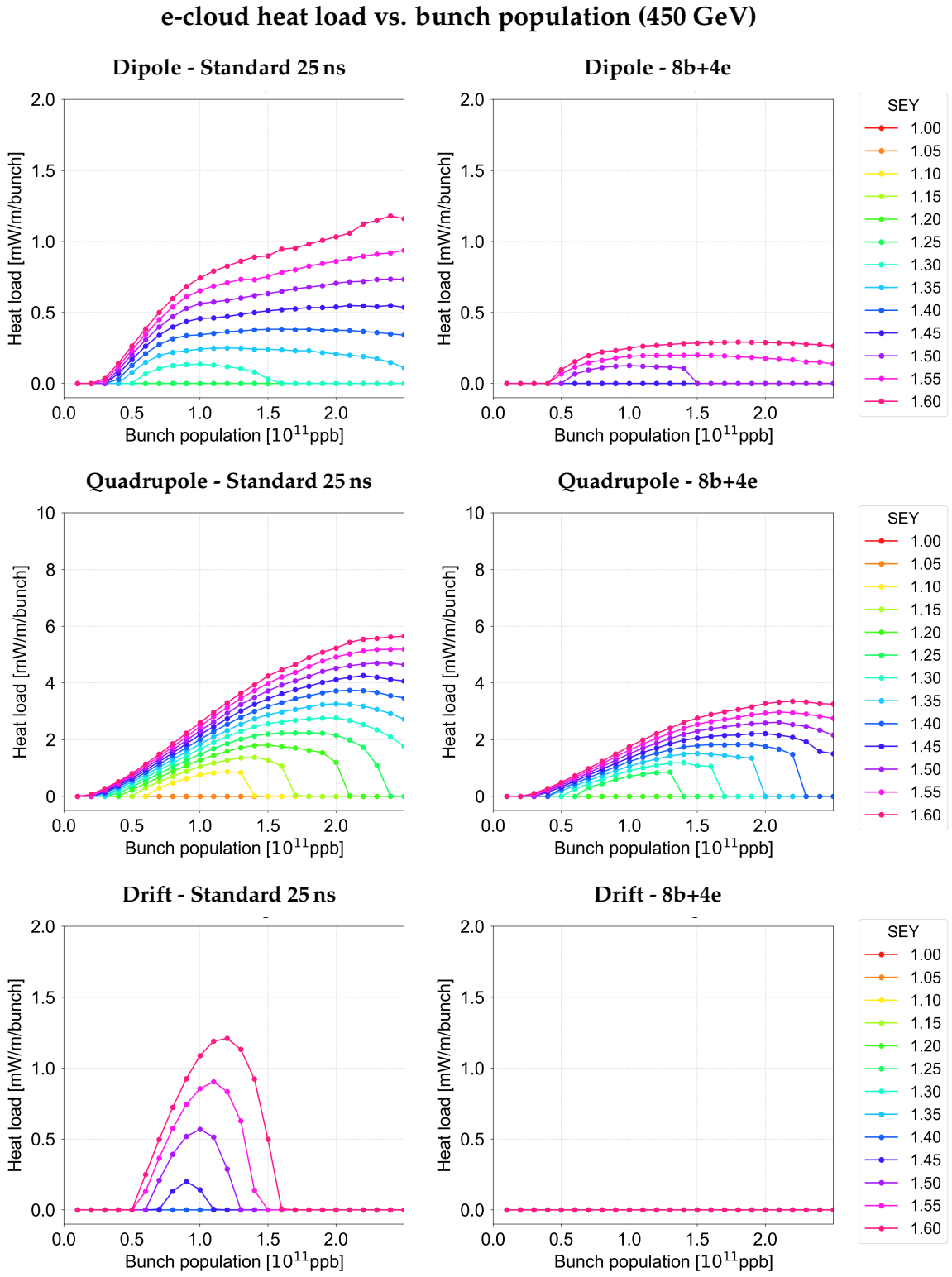

Figure 4: E-cloud induced heat load as a function of the bunch population for different values of the SEY parameter, in the arc dipole (top), quadrupole (middle) and drift (bottom) with the standard 25 ns (left) and the 8b+4e (right) beams at 450 GeV.

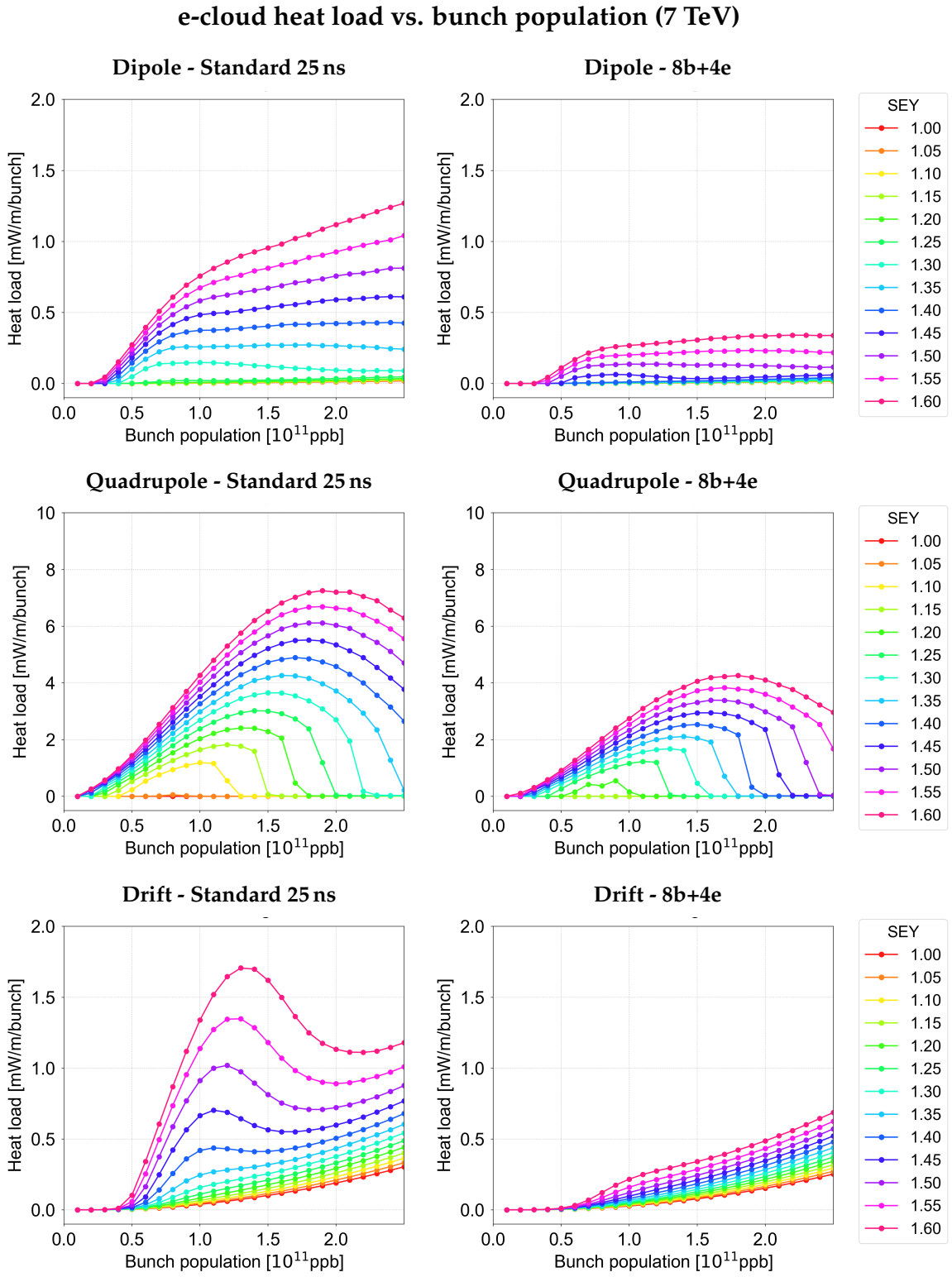

Figure 5: E-cloud induced heat load as a function of the bunch population for different values of the SEY parameter, in the arc dipole (top), quadrupole (middle) and drift (bottom) with the standard 25 ns (left) and the 8b+4e (right) beams at 7 TeV.

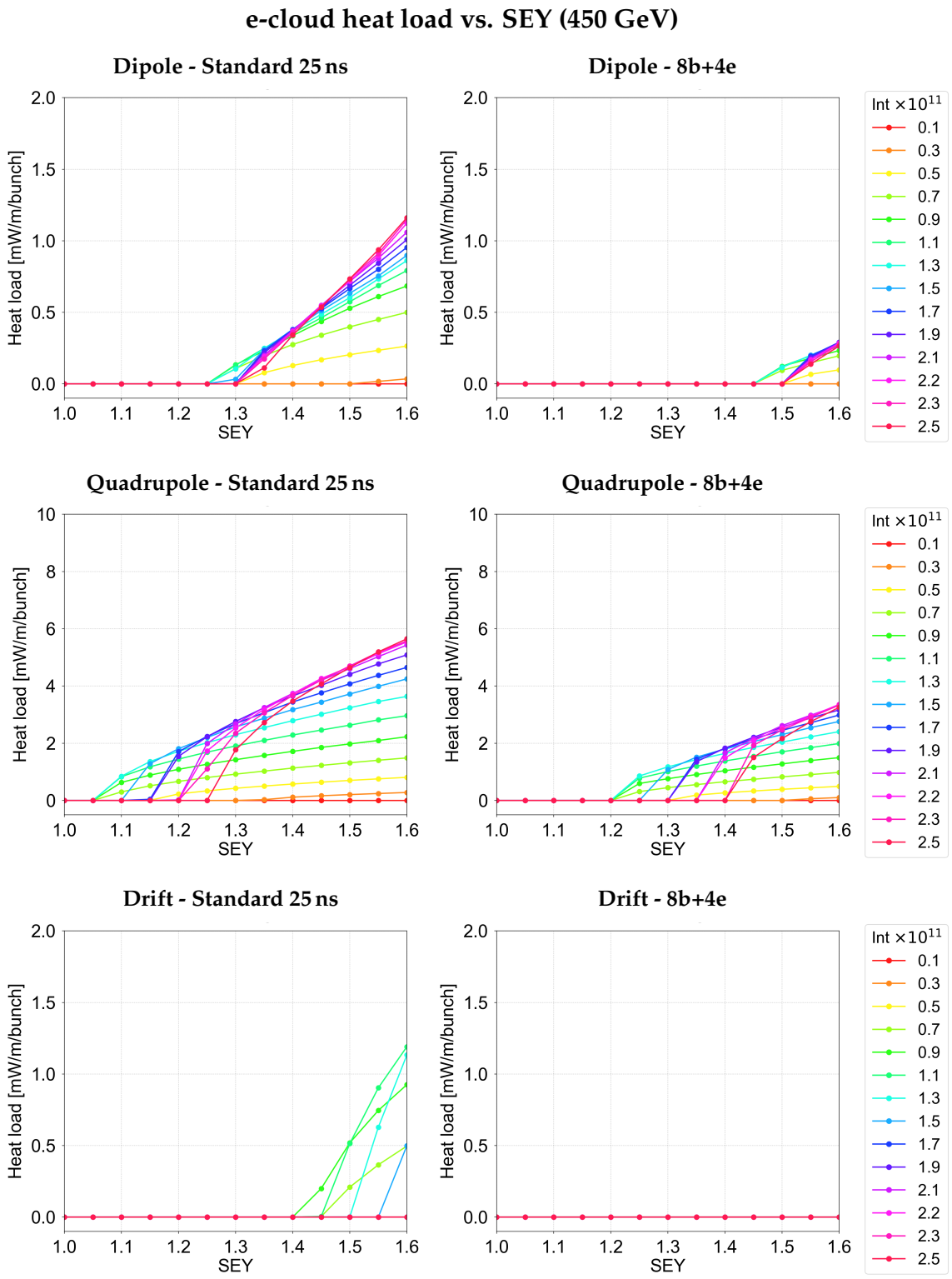

Figure 6: E-cloud induced heat load as a function of the SEY parameter for different values of the bunch population, in the arc dipole (top), quadrupole (middle) and drift (bottom) with the standard 25 ns (left) and the 8b+4e (right) beams at 450 GeV.

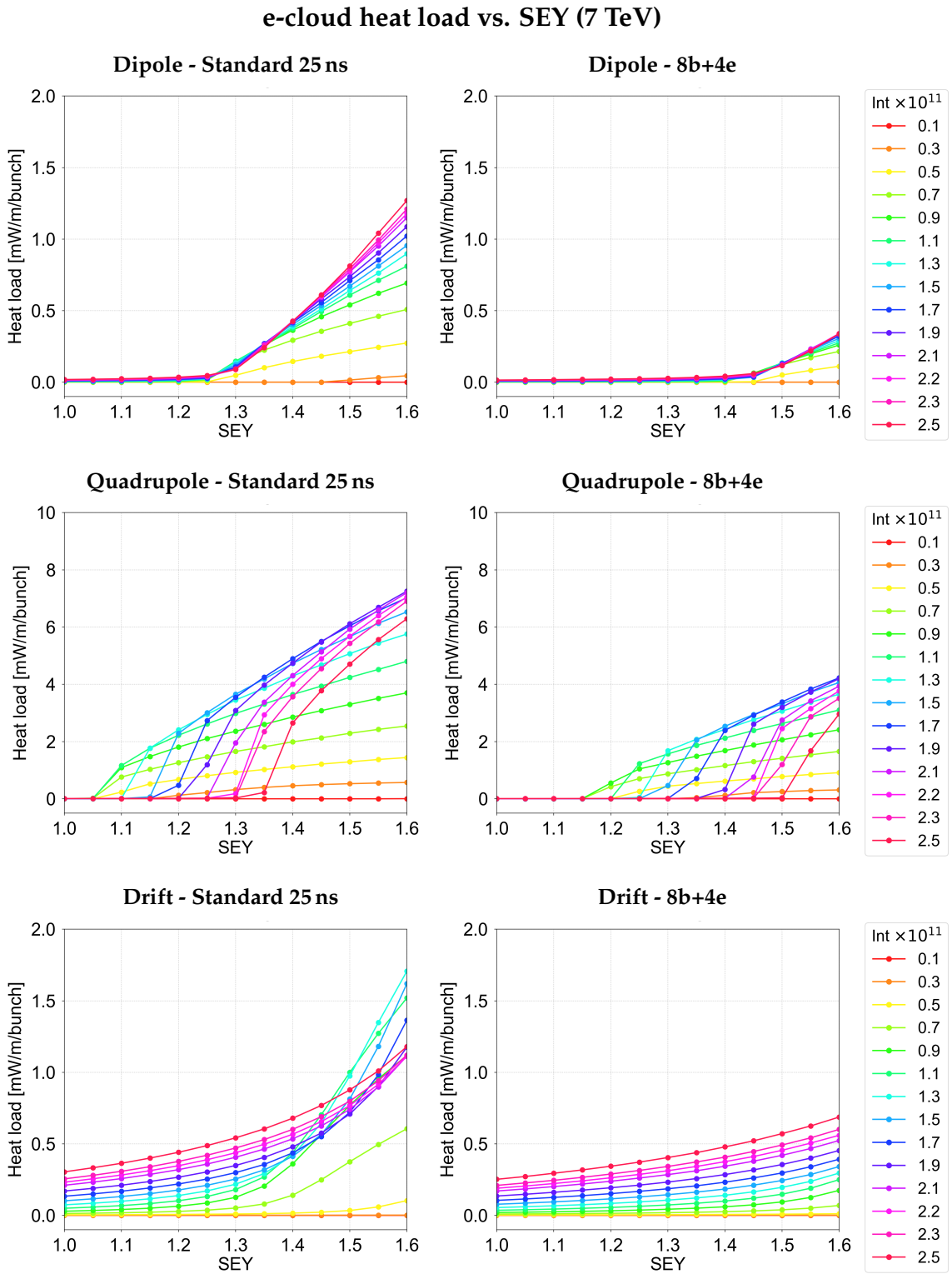

Figure 7: E-cloud induced heat load as a function of the SEY parameter for different values of the bunch population, in the arc dipole (top), quadrupole (middle) and drift (bottom) with the standard 25 ns (left) and the 8b+4e (right) beams at 7 TeV.

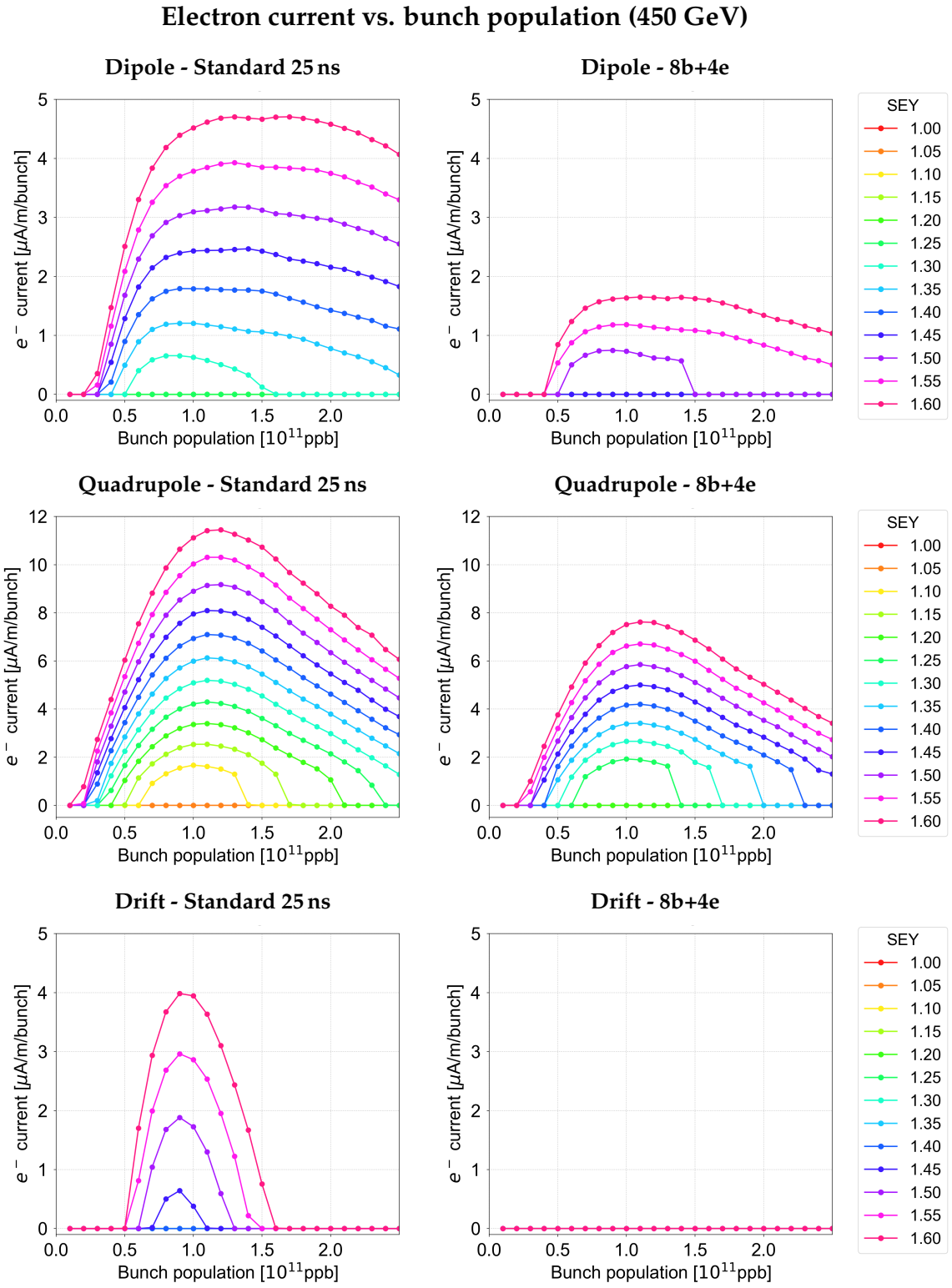

Figure 8: Electron current as a function of the bunch population for different values of the SEY parameter, in the arc dipole (top), quadrupole (middle) and drift (bottom) with the standard 25 ns (left) and the 8b+4e (right) beams at 450 GeV.

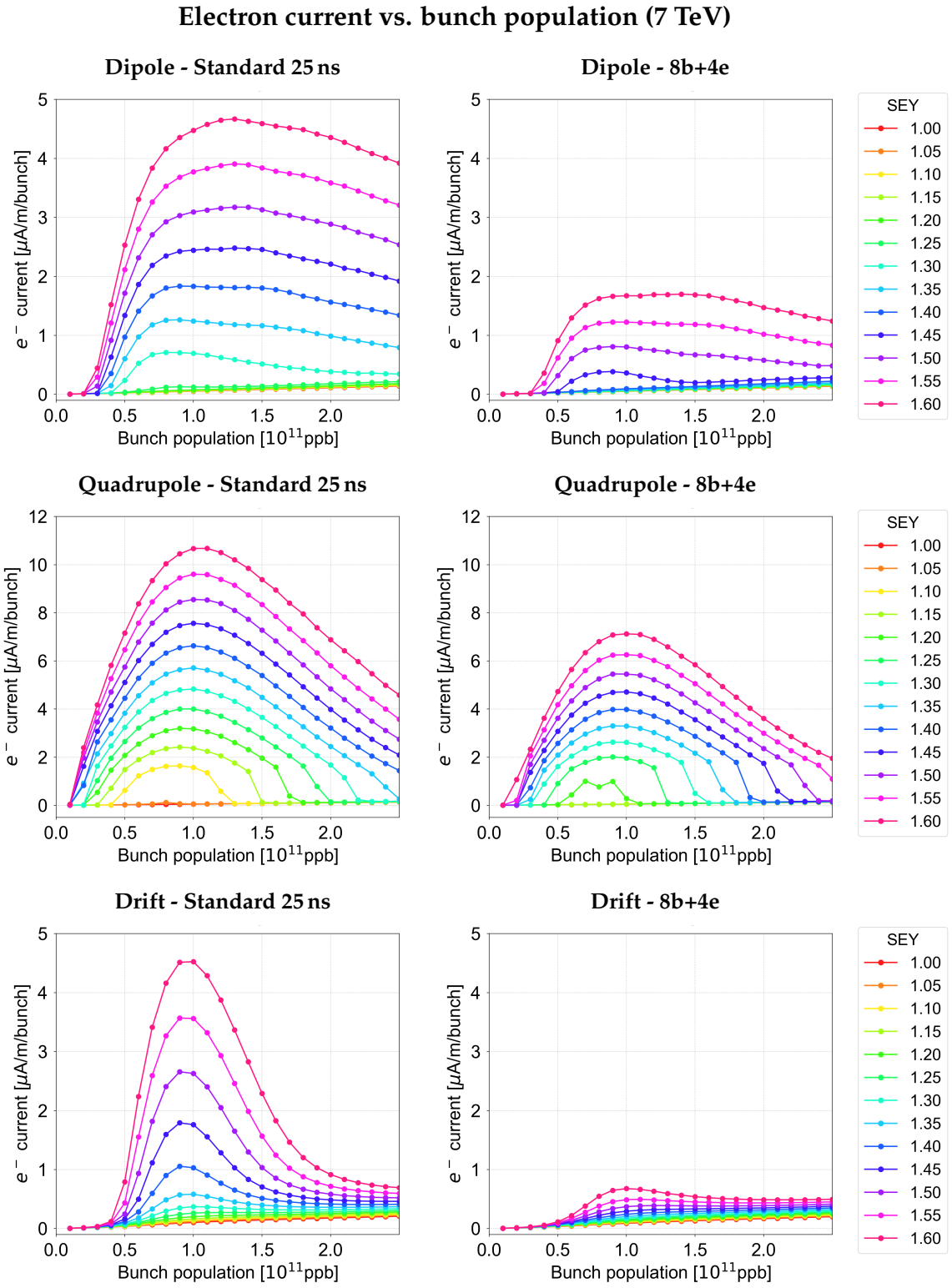

Figure 9: Electron current as a function of the bunch population for different values of the SEY parameter, in the arc dipole (top), quadrupole (middle) and drift (bottom) with the standard 25 ns (left) and the 8b+4e (right) beams at 7 TeV.

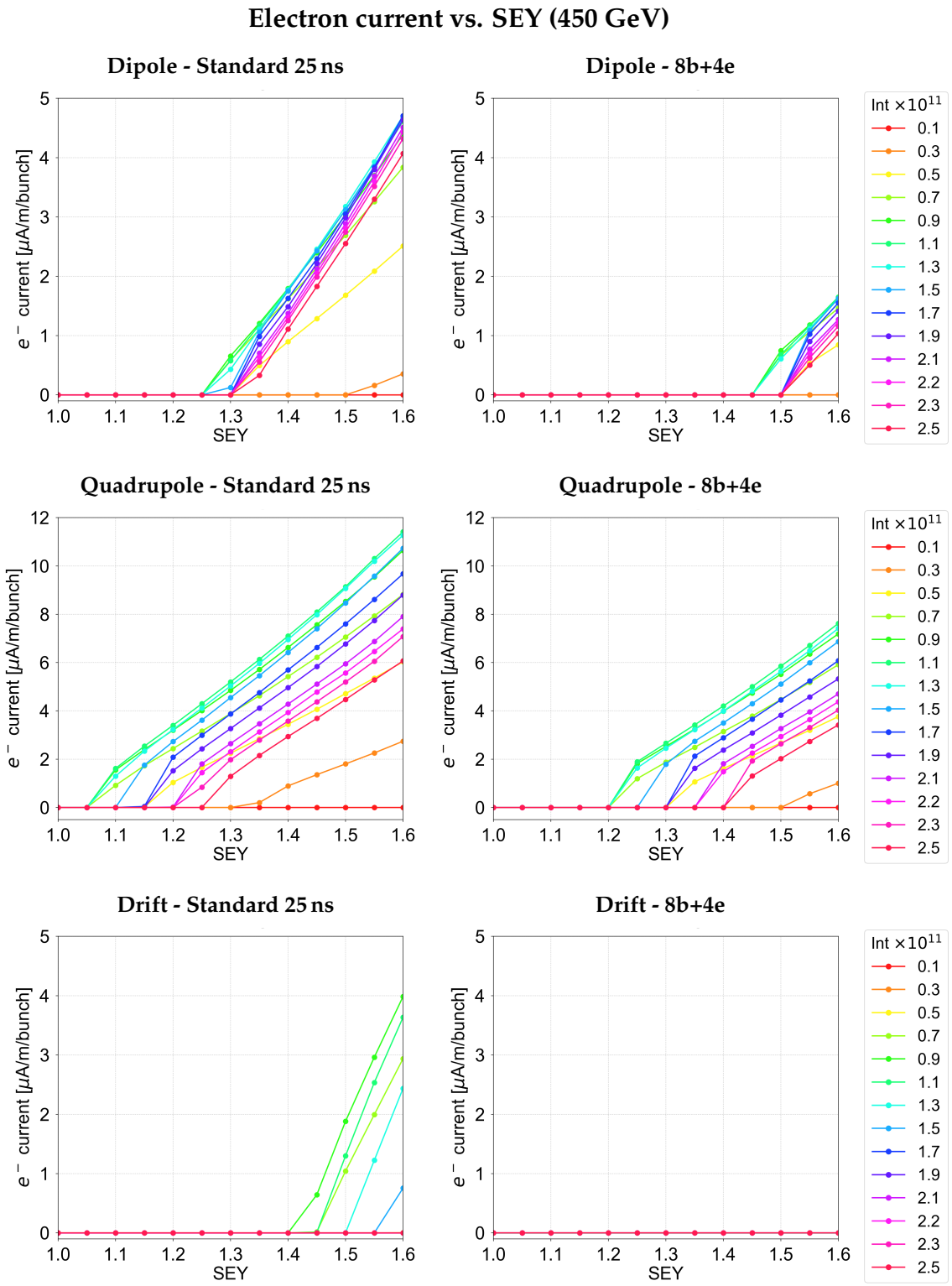

Figure 10: Electron current as a function of the SEY parameter for different values of the bunch population in the arc dipole (top), quadrupole (middle) and drift (bottom) with the standard 25 ns (left) and the 8b+4e (right) beams at 450 GeV.

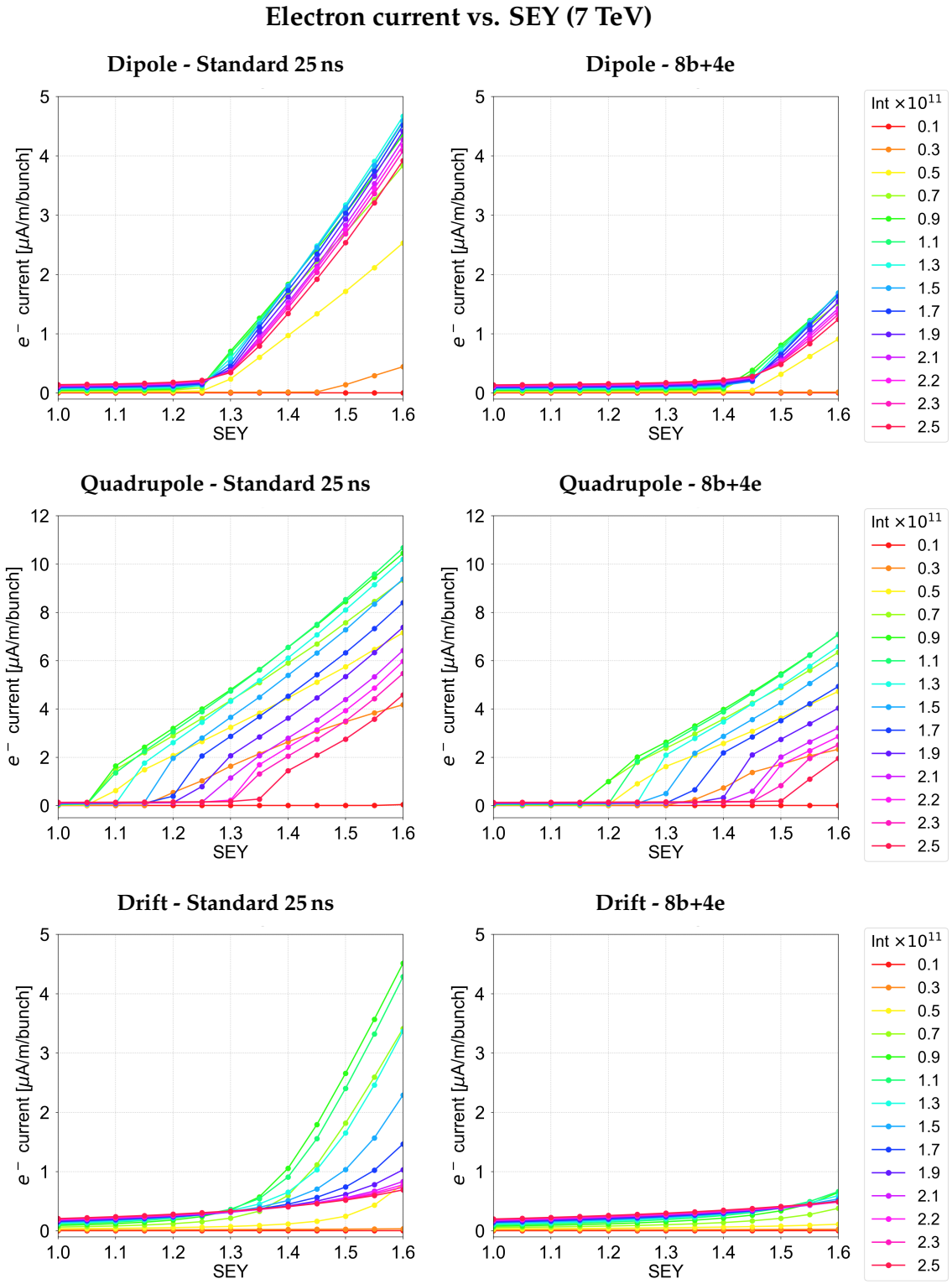

Figure 11: Electron current as a function of the SEY parameter for different values of the bunch population in the arc dipole (top), quadrupole (middle) and drift (bottom) with the standard 25 ns (left) and the 8b+4e (right) beams at 7 TeV.

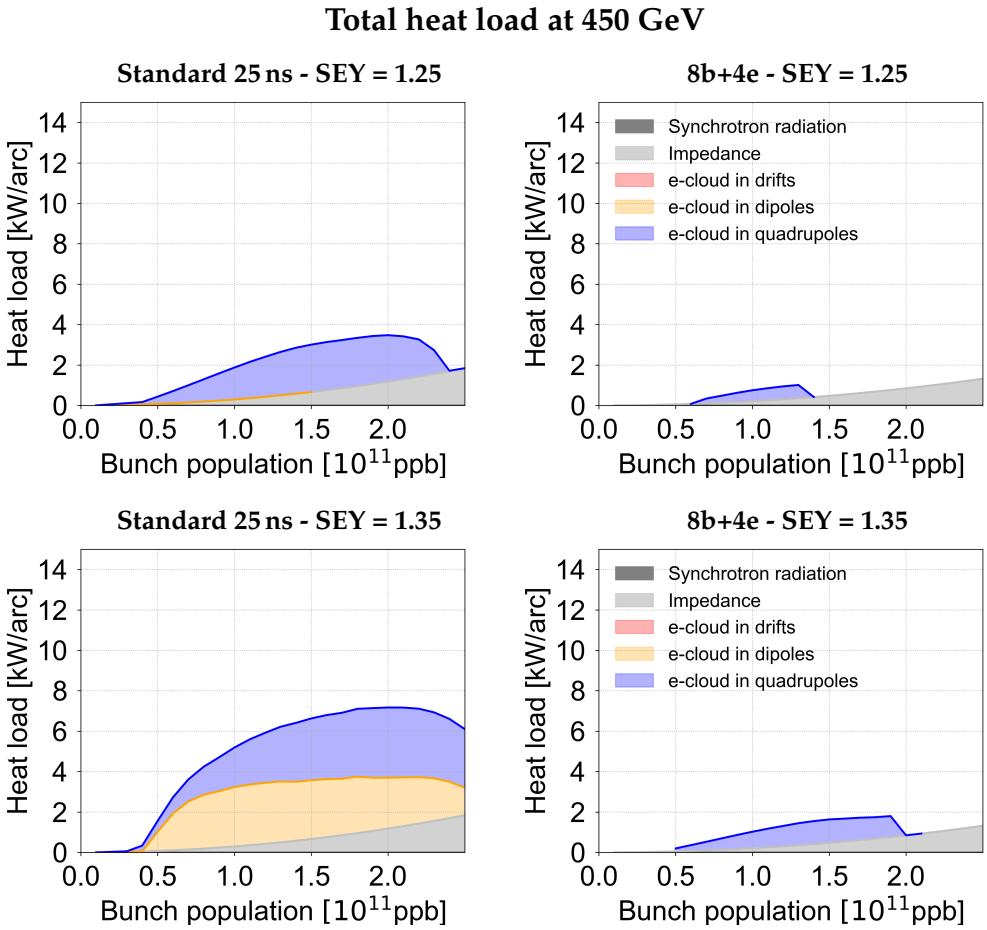

Figure 12: Total heat load as a function of the bunch population for SEY=1.25 (top) and SEY=1.35 (bottom) with the standard 25 ns (left) and the 8b+4e (right) beams at 450 GeV.

3 Total heat loads on the beam screens

The simulations presented in Sec. 2 allow computing the expected heat load for each arc, which can be compared against the cooling capacity available from the corresponding cryoplant.
By comparing build-up simulations against experimental data, it has been shown that the differences in heat load, which are observed among the LHC arcs, can be attributed to differences in SEY. In particular, the heat load measured in the arcs showing the lowest load is compatible with a SEY parameter of 1.25, while the heat load observed in the arcs showing the highest load is compatible with a SEY parameter of 1.35 [2].
Figures 12 and 13 show the total heat load expected at 450 GeV and at 7 TeV as a function of the bunch population, assuming these two values of the SEY parameter. The e-cloud contribution to the heat loads is computed from the simulations results presented in Sec. 2, rescaled to the total length of the magnets in each arc, as reported in Tab. 2. The length not occupied by the main magnets is counted as drift, as the effect of shorter corrector magnets was found to be negligible

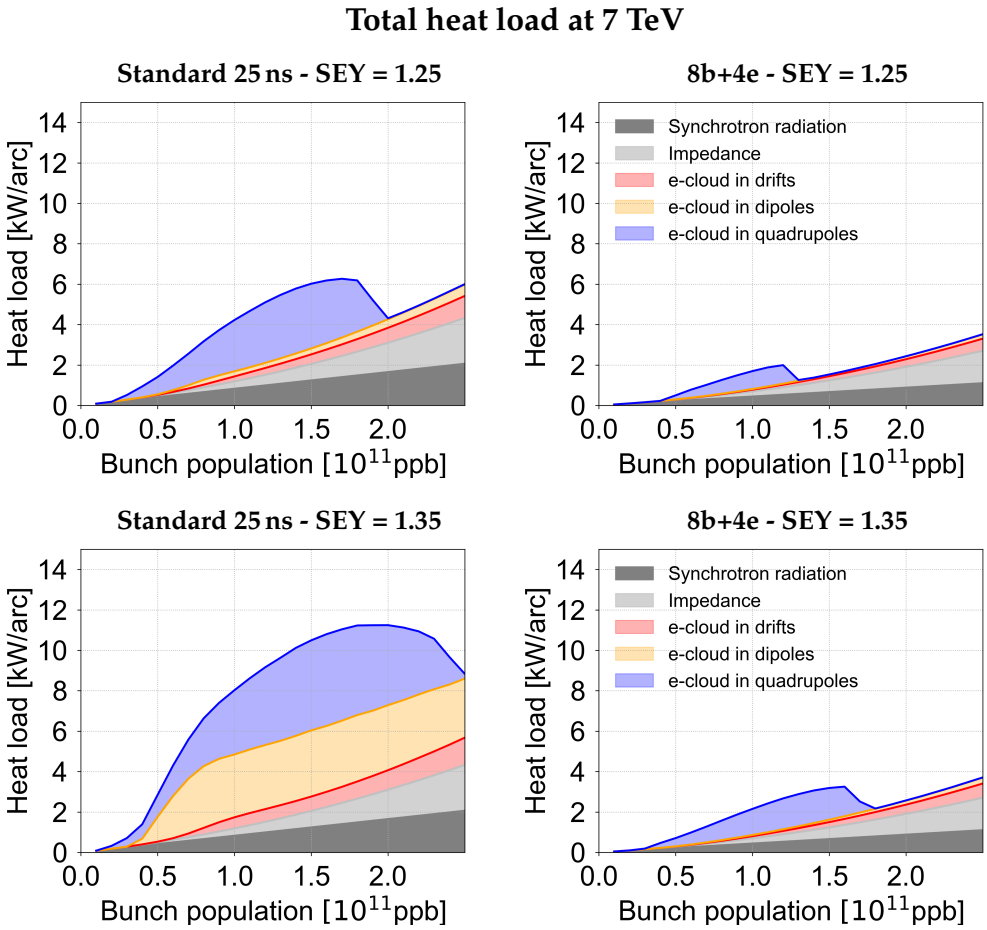

Figure 13: Total heat load as a function of the bunch population for SEY=1.25 (top) and SEY=1.35 (bottom) with the standard 25 ns (left) and the 8b+4e (right) beams at 7 TeV.

in previous studies [8].
The expected heat loads shown in Figs. 12 and 13 include the contributions from the impedance of the beam screen and from synchrotron radiation. These are estimated using the HeatLoadCalculator tool [13]. The model used to compute the impedance heating is described in detail in [14], and includes the dependence of the copper resistivity on the temperature and on the applied magnetic field as well as the effect of the longitudinal weld present in the LHC beam screens.
The power deposition from synchrotron radiation can be estimated analytically assuming that the radiation occurs in the arc dipoles only (the effect of lower field magnets is considered negligible) and that the power is entirely deposited within the arc length. Under these assumptions, the synchrotron radiation power for a

Table 2: Lengths of the LHC arc and its components

Arc length, m	2801
Total dipole length (one arc), m	2202
Total quadrupole length (one arc), m	194

single arc can be written as [15]:

$$P_{\text{arc}}^{\text{SR}} = \frac{1}{8}\frac{N q_e^2 \gamma^4 c}{3\varepsilon_0 \rho L}, \tag{1}$$

where N is the number of circulating protons, q_e is the elementary charge, γ is the relativistic factor, c is the speed of light, ϵ_0 is the vacuum permittivity, ρ is the bending radius of the arc main dipoles (2804 m) and L is the accelerator circumference (26659 m). The models used for the impedance and synchrotron radiation heating have been validated against experimental data using tests performed with large bunch spacing, during which the effect of the e-cloud can be considered negligible [3].
The design cooling capacity for the LHC arc beam screens is about 8 kW. Figure 13 shows that this would be sufficient to cope with HL-LHC intensities for the low-load arcs (SEY=1.25) while it would be insufficient for the high-load ones (SEY=1.35).
During Run 2, the LHC cryogenics has been operated in an optimized configuration (using one cold-compressor unit to serve two consecutive arcs) profiting from the lower-than-expected heat loads from the 1.9 K cold masses. The compatibility of this optimized configuration with the HL-LHC operational scenarios is being verified. With this optimized configuration, a higher cooling capacity of about 10 kW becomes available for the arc beam screens, which is very close to the maximum load expected in the high-load arcs during the HL-LHC luminosity fills [16].
In case the cooling capacity will not be sufficient, the heat loads will have to be mitigated using the 8b+4e scheme as clearly shown in Figs. 12 and 13. This has been confirmed experimentally at the LHC during Run 2 [3].

4 Hybrid schemes

The large heat load mitigation obtainable using 8b+4e beams instead of the 25 ns beams comes at expense of the number of circulating bunches, which is reduced by about 30 %.
In case the available cooling capacity is larger than required for the 8b+4e beam but not sufficient to operate with the full 25 ns beam, "hybrid schemes" can be used to maximize the number of bunches without exceeding the cooling capacity limit. This possibility has been tested experimentally at the LHC [17]. Examples of hybrid schemes, in which standard 25 ns bunch trains and 8b+4e bunch trains are used together within the same filling pattern, are shown in Figs. 14 and 15.
The number of injections needs to be minimized to avoid reductions in the number of bunches due to additional injection kicker gaps. Moreover, a four-fold symmetry needs to be present in the scheme to provide an adequate number of colliding bunch-pairs for all experiments. Taking these constraints into account, the required share between 25 ns and 8b+4e beams determines whether the mixing of the two beam types can be done in the LHC (as for the scheme in Fig. 14) or needs to be made already in the SPS ring (as for the scheme in Fig. 15).

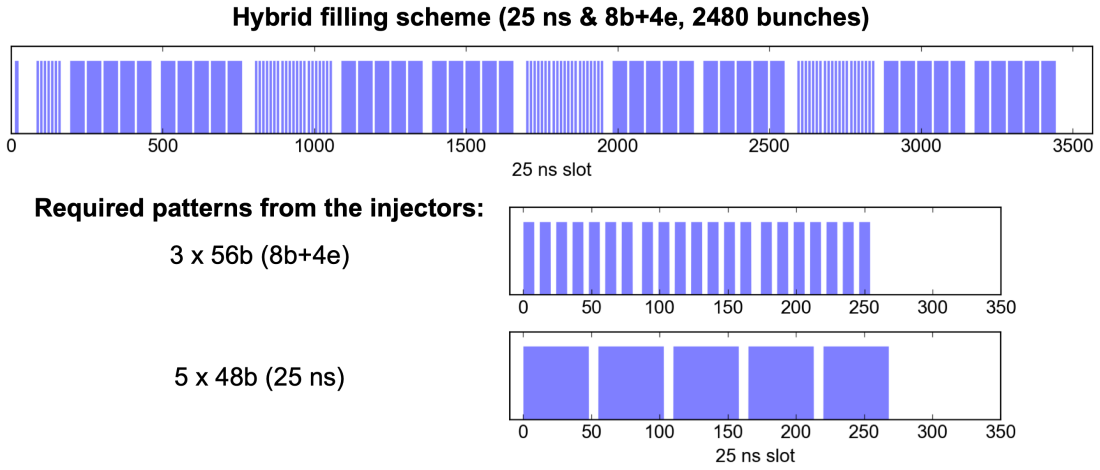

Figure 14: Example of hybrid scheme with 2480 bunches. The blue background marks the filled bunch slots.

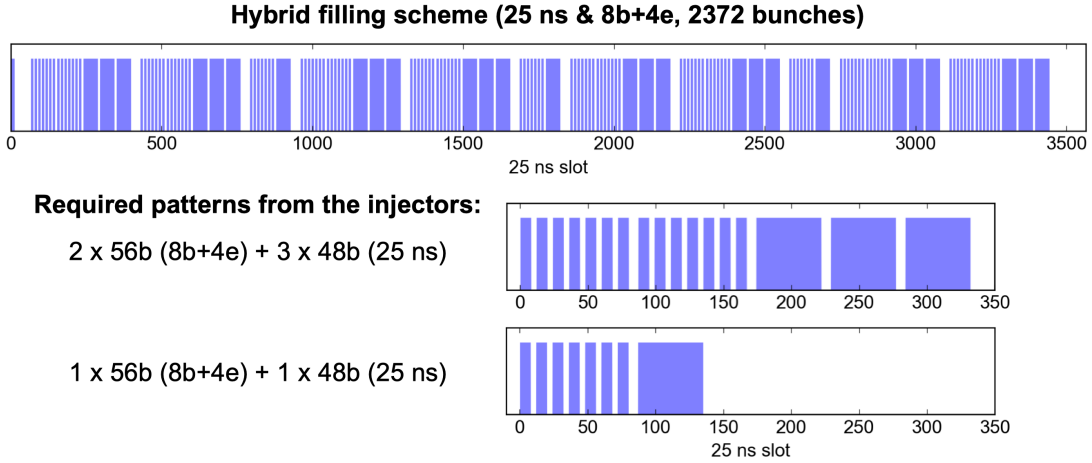

Figure 15: Example of hybrid scheme with 2372 bunches. The blue background marks the filled bunch slots.

The share between 8b+4e and standard 25 ns beams that is required to achieve a certain target heat load W_{hybrid} can be calculated, given the heat load $W_{25\text{ns}}$ that would be produced by the full standard 25 ns beam, using a simple analytic model.
We call $L_{8\text{b4e}}$ the relative loss in number of bunches between the "pure" 8b+4e scheme (in Fig. 2) and the standard 25 ns scheme (in Fig. 1):

$$L_{8\text{b4e}} = \frac{N_{25\text{ns}} - N_{8\text{b4e}}}{N_{25\text{ns}}}\,, \tag{2}$$

where $N_{25\text{ns}}$ is the total number of bunches for the standard 25 ns filling scheme and $N_{8\text{b4e}}$ is the total number of bunches for the 8b+4e scheme.
For a certain hybrid scheme, we define $f_{8\text{b4e}}$ as the fraction of 25 ns trains replaced by 8b+4e trains, so that the total number of circulating bunches is given by:

$$N_{\text{hybrid}} = N_{25\text{ns}}\left(1 - f_{8\text{b4e}} L_{8\text{b4e}}\right)\,. \tag{3}$$

We call w^{isr} the heat load per bunch generated by impedance and synchrotron radiation (which is independent on the bunch pattern), and we call $w^{\mathrm{EC}}_{25\mathrm{ns}}$ and $w^{\mathrm{EC}}_{8\mathrm{b4e}}$ the heat load per bunch generated by e-cloud for the 25 ns and the 8b+4e trains respectively.
We define S^{EC} as the e-cloud suppression factor between the two schemes:

$$S^{\mathrm{EC}} = \frac{w^{\mathrm{EC}}_{8\mathrm{b4e}}}{w^{\mathrm{EC}}_{25\mathrm{ns}}} \,. \tag{4}$$

Figure 16 shows the e-cloud suppression factor between the 8b+4e and the standard 25 ns beams for SEY = 1.35, inferred from the simulations presented in Sec. 2.

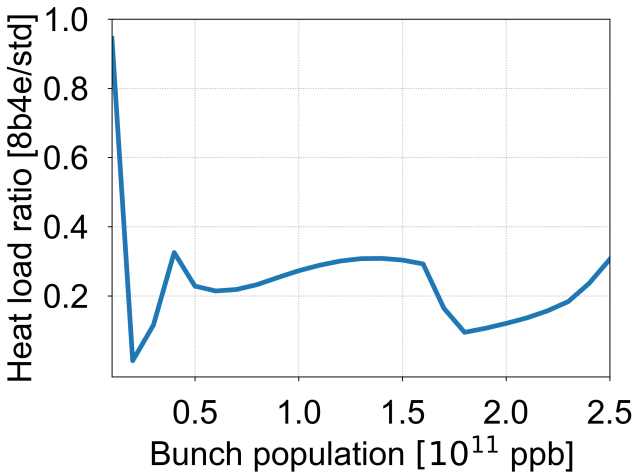

Figure 16: The e-cloud suppression factor between the 8b+4e and the standard 25 ns beams at 7 TeV for SEY = 1.35 (based on simulations presented in Sec.2).

The heat load generated by the hybrid scheme can be written as:

$$W_{\mathrm{hybrid}} = N_{25\mathrm{ns}} w^{\mathrm{isr}} \left(1 - f_{8\mathrm{b4e}} L_{8\mathrm{b4e}}\right) + N_{25\mathrm{ns}} w^{\mathrm{EC}}_{25\mathrm{ns}} \left(1 - f_{8\mathrm{b4e}}\right) + N_{25\mathrm{ns}} w^{\mathrm{EC}}_{8\mathrm{b4e}} f_{8\mathrm{b4e}} \left(1 - L_{8\mathrm{b4e}}\right) \,. \tag{5}$$

This can be rewritten as:

$$W_{\mathrm{hybrid}} = W_{25\mathrm{ns}} - f_{8\mathrm{b4e}} \left[W_{25\mathrm{ns}} - W^{\mathrm{isr}}_{25\mathrm{ns}} \left(1 - L_{8\mathrm{b4e}}\right) - \left(W_{25\mathrm{ns}} - W^{\mathrm{isr}}_{25\mathrm{ns}} \right) S^{\mathrm{EC}} \left(1 - L_{8\mathrm{b4e}}\right) \right] \,, \tag{6}$$

where $W_{25\mathrm{ns}}$ is the total heat load generated by the full standard 25 ns scheme:

$$W_{25\mathrm{ns}} = N_{25\mathrm{ns}} \left(w^{\mathrm{isr}} + w^{\mathrm{EC}}_{25\mathrm{ns}} \right) \tag{7}$$

and $W^{\mathrm{isr}}_{25\mathrm{ns}}$ is the heat load generated by impedance and synchrotron radiation for the full standard 25 ns scheme:

$$W^{\mathrm{isr}}_{25\mathrm{ns}} = N_{25\mathrm{ns}} w^{\mathrm{isr}} \,. \tag{8}$$

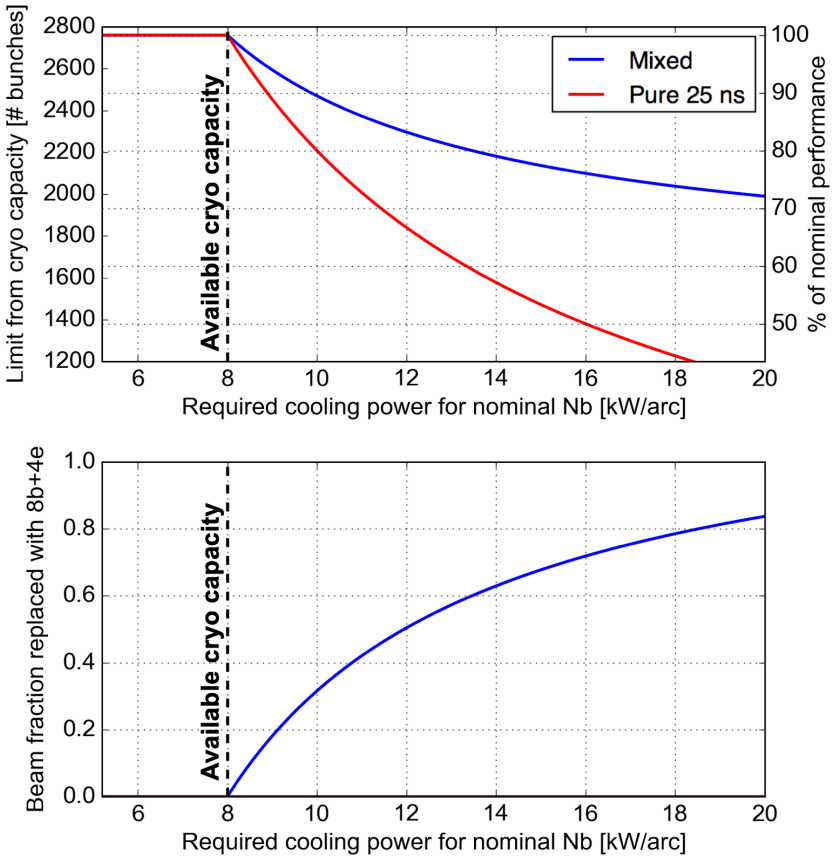

Figure 17: Bottom: optimal share f_{8b4e} for a target heat load W_{hybrid}=8 kW, as a function of the cooling capacity required by the full 25 ns scheme. Top: achievable number of bunches with the standard 25 ns and with the hybrid schemes.

From Eq. 6 we can write a relation providing the required 8b+4e share (f_{8b4e}) for an assigned target heat load W_{hybrid}:

$$f_{8b4e} = \frac{W_{25ns} - W_{hybrid}}{W_{25ns} - W_{25ns}^{isr}\left(1 - L_{8b4e}\right) - \left(W_{25ns} - W_{25ns}^{isr}\right) S^{EC}\left(1 - L_{8b4e}\right)} . \quad (9)$$

The bottom plot in Fig. 17 shows the optimal share f_{8b4e} for a target heat load W_{hybrid}=8 kW, as a function of the cooling capacity required by the full 25 ns scheme. The corresponding achievable number of bunches is shown in Fig. 17 (top), where it is compared against the number of bunches required to match the target heat load when using the standard 25 ns beam alone. This clearly shows the advantage of the hybrid scheme in terms of achievable performance.
The curves in Fig. 17 are calculated assuming S^{EC}=0.3, which was measured at the LHC with nominal bunch population [18]. Based on the simulations described in the previous sections, S^{EC}=0.3 is also the largest value to be expected for the high-load arcs in the range of bunch populations of interest for HL-LHC, as shown in Fig. 16.

5 Summary and conclusions

The beam-induced heat loads on the beam screens of the cold magnets and drifts of the HL-LHC arcs have been estimated taking into account the contributions from e-cloud effects, impedance and synchrotron radiation. The e-cloud estimates are based on the results of macroparticle simulations performed with the PyECLOUD code, whereas the impedance and the synchrotron radiation contributions are estimated from analytical models.
Different SEY are considered for the different arcs, in order to account for the different heat loads observed in the eight LHC arcs. The design cooling capacity of 8 kW/arc would be sufficient to cope with HL-LHC intensities for the low-load arcs (SEY=1.25) while it would be insufficient for the high-load ones (SEY=1.35).
During Run 2, the LHC cryogenics has been operated in an optimized configuration providing a higher cooling capacity of about 10 kW/arc. This is very close to the maximum load expected in the high-load arcs during the HL-LHC luminosity fills.
In case the cooling capacity will not be sufficient, the heat loads can be mitigated using the 8b+4e scheme. If the available cooling capacity is larger than required for the 8b+4e beam but not sufficient to operate with the full 25 ns beam, "hybrid schemes" can be used to maximize the number of bunches without exceeding the limit defined by the cryogenic capacity.

Acknowledgments

The authors would like to thank G. Arduini, P. Dijkstal, L. Mether, E. Métral, G. Rumolo, and E. Wulff for their important input and support to the presented studies.

Appendix: Electron distribution and energy spectrum

Figures 18 – 24 illustrate additional results obtained from the e-cloud build-up simulations presented in Sec. 2, concerning in particular the spacial distribution of the electrons and their energy at the moment of their impact on the chamber's wall.
In the dipole magnets the electrons concentrate in two vertical stripes, which move away from the beam for larger bunch populations, as illustrated in Figs. 18 and 19. These are the regions in which the multipacting is more efficient, since the impacting electrons have energies close to the maximum of the SEY curve. These features could be observed experimentally at the SPS using strip-detectors to measure the horizontal profile of the e-cloud [19, 20].
In the quadrupole magnet the electrons are confined by the magnetic field lines and concentrate in a cross-shaped region originating from the magnet poles, as illustrated in Fig. 21. This strongly increases the electron density at the beam location compared to the case of dipole and of the drift. Also this distribution could be measured experimentally at the SPS [21].
Figures 20, 22 and 24 show the energy spectrum of the electrons impacting on the chamber's surface for different values of the bunch population. Similar features can be noticed for all devices. All curves have a peak at very low energy, which corresponds to electrons that hit the wall before being accelerated by a passing bunch. A second maximum can be observed at larger energies, corresponding to electrons that are accelerated by the beam. This maximum shifts towards higher energy for increasing bunch population.

Dipole magnet

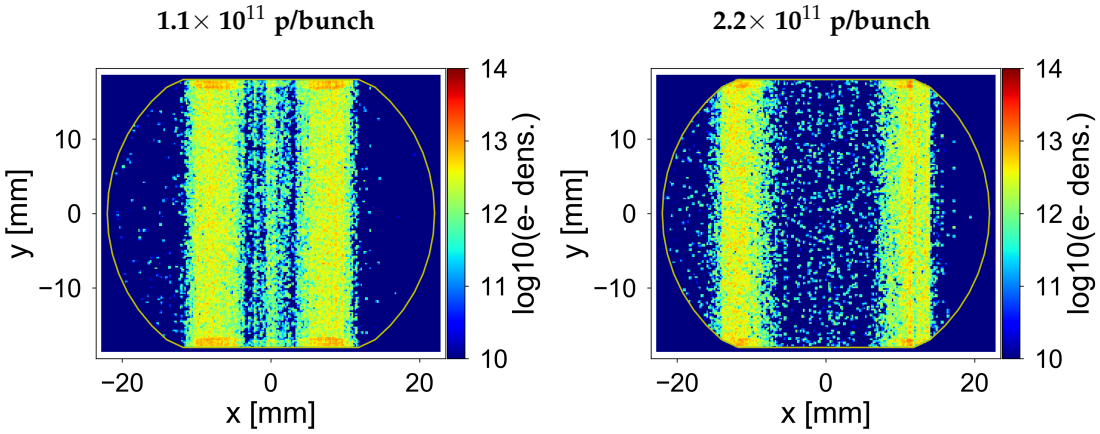

Figure 18: Snapshot of the electron distribution for two different values of the bunch population (standard 25 ns beam, 7 TeV, SEY=1.5).

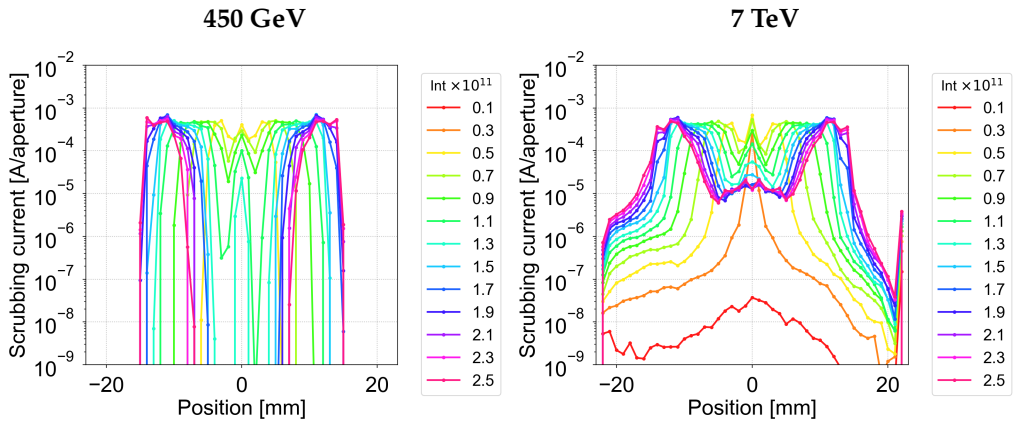

Figure 19: Horizontal distribution of the electron current in the arc dipole (standard 25 ns beam, SEY=1.5).

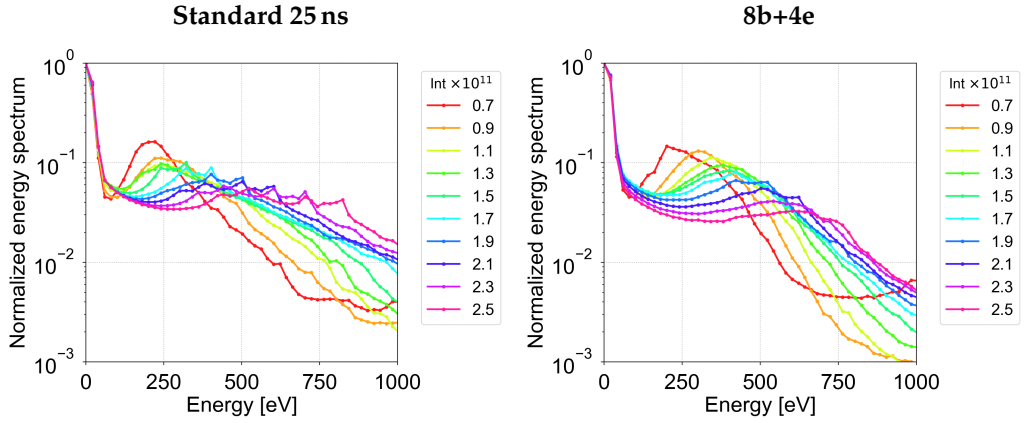

Figure 20: Normalized energy spectrum of the electrons impacting the wall (7 TeV, SEY=1.5).

Quadrupole magnet

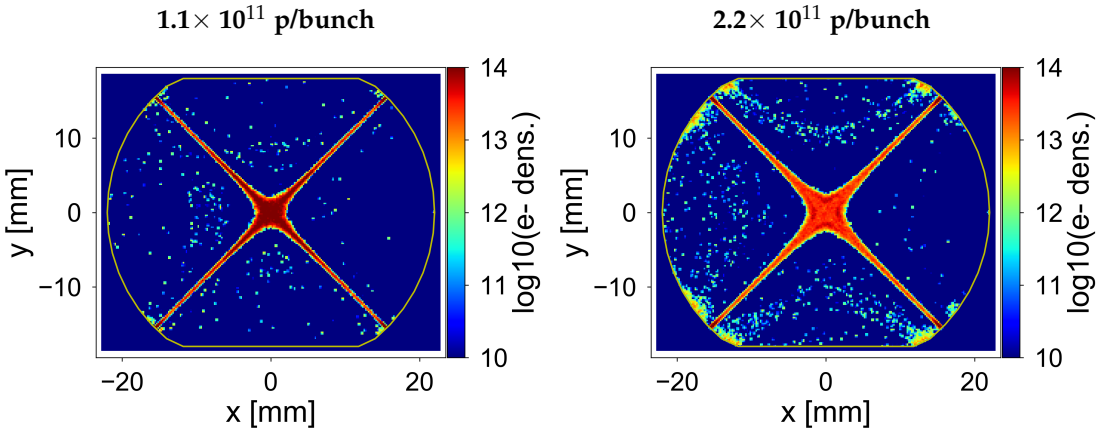

Figure 21: Snapshot of the electron distribution for two different values of the bunch population (standard 25 ns beam, 7 TeV, SEY=1.5).

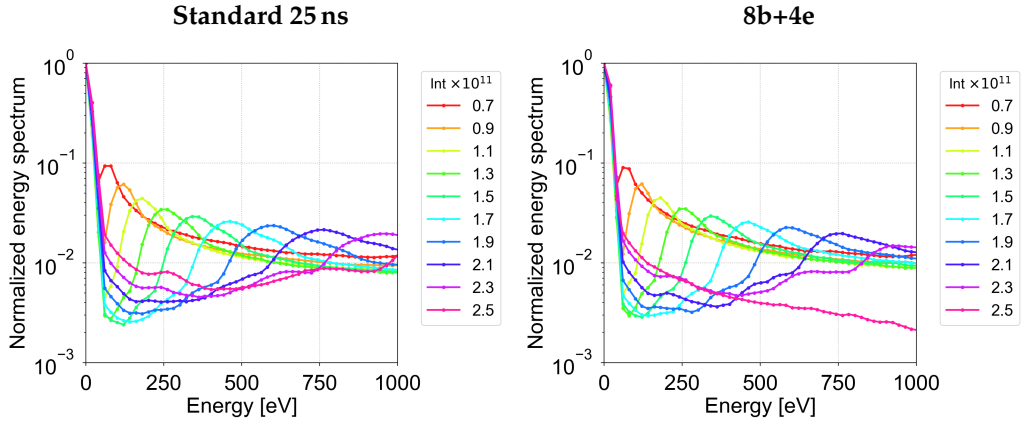

Figure 22: Normalized energy spectrum of the electrons impacting the wall (7 TeV, SEY=1.5).

Drift section

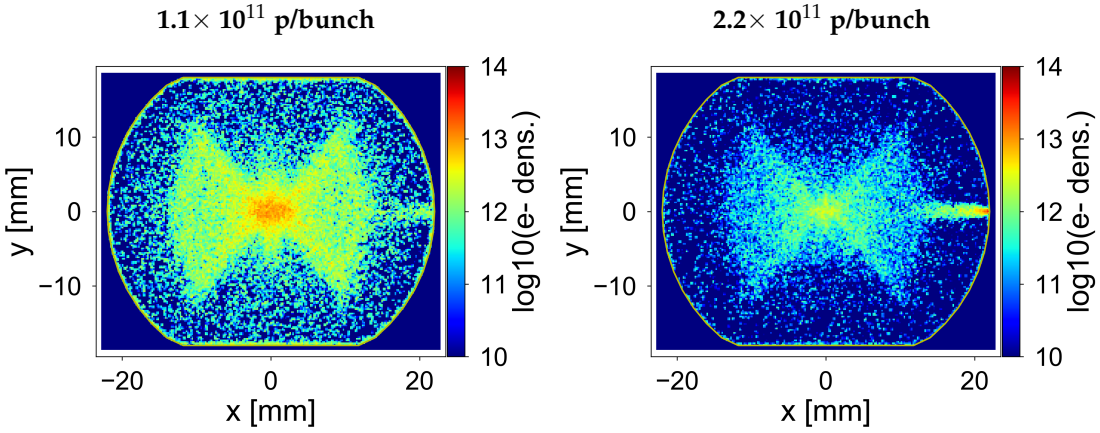

Figure 23: Snapshot of the electron distribution for two different values of the bunch population (standard 25 ns beam, 7 TeV, SEY=1.5).

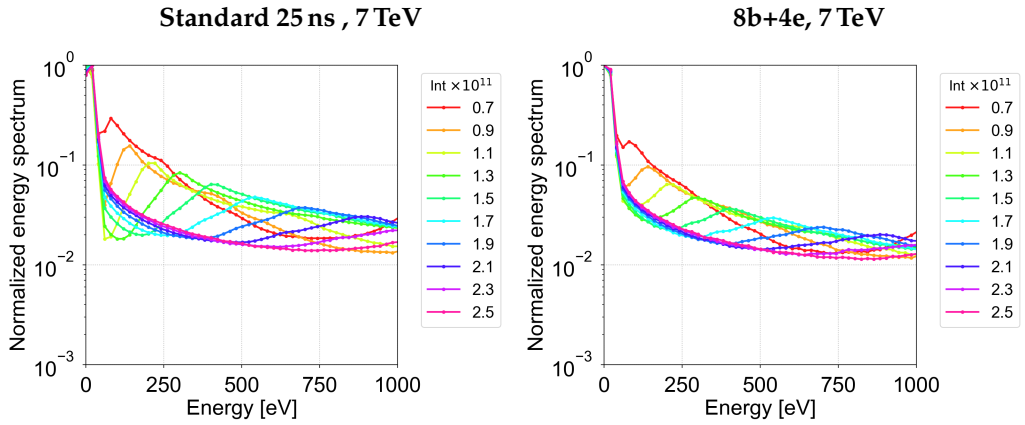

Figure 24: Normalized energy spectrum of the electrons impacting the wall (7 TeV, SEY=1.5).

References

[1] G. Iadarola *et al.*, "Electron cloud and heat loads in run 2," *in Proc. 2019 Evian Workshop on LHC beam operation, Evian Les Bains, France, January 2019.* https://indico.cern.ch/event/751857/timetable/.

[2] G. Skripka, G. Iadarola, L. Mether, G. Rumolo, E. Wulff, and P. Dijkstal, "Comparison of electron cloud build-up simulations against heat load measurements for the LHC arcs with different beam configurations," in *Proc. 10th Int. Particle Accelerator Conf. (IPAC'19), Melbourne, Australia, May 2019, pp. 3232–3235.*

[3] G. Iadarola, G. Rumolo, P. Dijkstal, and L. Mether, "Analysis of the beam induced heat loads on the LHC arc beam screens during Run 2," *CERN-ACC-NOTE-2017-0066*, December 2017.

[4] G. Apollinari, I. Bejar Alonso, O. Bruning, P. Fessia, M. Lamont, L. Rossi, and L. Tavian, *High-Luminosity Large Hadron Collider (HL-LHC): Technical Design Report V. 0.1*. CERN Yellow Reports: Monographs 4/2017, Geneva: CERN, 2017.

[5] E. Metral *et al.*, "Update of the HL-LHC operational scenarios for proton operation," *CERN-ACC-NOTE-2018-0002*, January 2018.

[6] G. Iadarola, E. Belli, K. Li, L. Mether, A. Romano, and G. Rumolo, "Evolution of Python Tools for the Simulation of Electron Cloud Effects," in *Proc. 8th Int. Particle Accelerator Conf. (IPAC'17), Copenhagen, Denmark, May, 2017, pp. 3803–3806.*

[7] G. Iadarola, H. Bartosik, K. Li, L. Mether, A. Romano, G. Rumolo, and M. Schenk, "Performance limitations from electron cloud in 2015," in *Proc. of 6th Evian Workshop on LHC beam operation, Evian Les Bains, France, December, 2015, pp.101–110.*

[8] P. Dijkstal, G. Iadarola, L. Mether, and G. Rumolo, "Simulation studies on the electron cloud build-up in the elements of the LHC Arcs at 6.5 TeV," *CERN-ACC-NOTE-2017-0057*, October 2017.

[9] R. Cimino, I. Collins, M. Furman, M. Pivi, F. Ruggiero, G. Rumolo, and F. Zimmermann, "Can low-energy electrons affect high-energy physics accelerators?," *Physical Review Letters*, vol. 93, 06 2004.

[10] L. Giacomel, "A study on the e-cloud saturation mechanism," *Presentation at the E-cloud meeting 67, 10 May 2019, CERN.* https://indico.cern.ch/event/811014/.

[11] P. Dijkstal, "Electron cloud buildup studies for the LHC," *CERN-THESIS-2017-180*, September 2017.

[12] M. G. Billing, J. Conway, E. E. Cowan, J. A. Crittenden, W. Hartung, J. Lanzoni, Y. Li, C. S. Shill, J. P. Sikora, and K. G. Sonnad, "Measurement of electron trapping in the Cornell Electron Storage Ring," *Phys. Rev. ST Accel. Beams*, vol. 18, p. 041001, April 2015.

[13] G. Iadarola and P. Dijkstal, "Heat load calculators for the Large Hadron Collider," 2016.
https://github.com/giadarol/HeatLoadCalculators.

[14] G. Iadarola, E. Metral, and G. Rumolo, "Beam induced heat loads on the beam-screens of the twin-bore magnets in the IRs of the HL-LHC," *CERN-ACC-2016-0112*, September 2016.

[15] A. Hofmann, *The Physics of Synchrotron Radiation*. Cambridge Monographs on Particle Physics, Nuclear Physics and Cosmology, Cambridge University Press, 2004.

[16] K. Brodzinski, "Measurement of available beam screen cooling capacity on cryoplants," *Presentation at the LHC Machine Committee, 10 April 2019, CERN.*
https://indico.cern.ch/event/812689/.

[17] G. Iadarola, H. Bartosik, E. Belli, L. R. Carver, P. Dijkstal, K. S. B. Li, L. Mether, A. Romano, and G. Rumolo, "MD421: Electron cloud studies on 25 ns beam variants (BCMS, 8b+4e)," *CERN-ACC-NOTE-2017-0028*, March 2017.

[18] G. Iadarola, "Digesting the LIU high brightness beam: is this an issue for HL-LHC?," *Presentation at the LHC Performance Workshop 2018, 31 January 2018, Chamonix*.
https://indico.cern.ch/event/676124/.

[19] J. M. Jimenez, G. Arduini, P. Collier, G. Ferioli, B. Henrist, N. Hilleret, L. Jensen, K. Weiss, and F. Zimmermann, "Electron cloud with LHC-type beams in the SPS: A review of three years of measurements," *LHC-Project-Report-632*, April 2003.

[20] H. Bartosik, G. Iadarola, G. Rumolo, F. Caspers, M. Driss Mensi, S. Federmann, M. Holz, H. Neupert, and M. Taborelli, "Electron Cloud and Scrubbing Studies for the SPS in 2012," *CERN-ATS-Note-2013-019 MD*, April 2013.

[21] J. M. Jimenez, "E-Cloud diagnostics and observations," in *Proc. Final CARE-HHH Workshop on Scenarios for the LHC Upgrade and FAIR, Chavannes-de-Bogis, Switzerland, November 2008, pp.120–127.*